Wearable Electrically Small Loop Antennas for Monitoring Joint Flexion and Rotation

Vigyanshu Mishra, *Student Member, IEEE*, and Asimina Kiourti, *Senior Member, IEEE*

***Abstract*— Wearable electrically small loop antennas (ESLAs) are introduced to monitor joint flexion and rotation while overcoming limitations in the state-of-the-art. The reported approach is not restricted to laboratory environments, does not suffer from integration drift and line-of-sight, and does not impede natural movement. Our previous work introduced wrap-around coils that addressed the challenges above but were limited to monitoring joint flexion. In contrast, a new class of ESLAs is herewith proposed, placed longitudinally across the joint, and operated at 34 MHz to monitor both flexion and rotation. An added advantage versus our previous design is a remarkable improvement in flexion angle resolution: the transmission coefficient dynamic range for 0°–100° flexion improves by 18.8 dB in this article. Two ESLAs are shown to accurately detect flexion/rotation for angular resolutions up to 10°. However, if higher resolution is desired, ambiguities arise. To tackle this, a three-ESLA system with integrated post-processing is proposed that achieves resolution as high as 2°. Simulations and *in vitro* experiments are in excellent agreement. Guidelines for system design suited to diverse applications are discussed, and conformance with safety standards is ensured. In future, ESLAs can be seamlessly integrated in garments, enabling transformative benefits to healthcare, sports, and beyond.**

***Index Terms*— Bioelectromagnetics, electrically small loop antenna (ESLA), joint flexion and rotation, wearables.**

I. INTRODUCTION

HUMAN joints can flex and rotate, allowing for various complex movements. The vision of monitoring such movements in real time, seamlessly, without obstructing natural movement, and in the individual's natural environment, may ultimately open doors for innumerous applications. Examples include monitoring of motor disabling conditions [caused due to Parkinson's, traumatic brain injury (TBI), physical injury, etc.] [1], [2], gesture recognition and human–machine interfaces for virtual reality applications [3], [4], monitoring of athletes' performance [5], collection of baseline data from healthy individuals, and better understanding of obscure motor disabling diseases from a research perspective.

Currently, there are several technologies available to monitor joint motion. Despite having certain benefits, they suffer from inherent disadvantages which do not allow motion capture per the vision outlined above (Table I). Specifically, optical camera-based systems that rely on retro-reflective markers [6], [7] as well as their markerless versions [8], [9] are restricted to laboratory environments and line of sight. Antenna and other electromagnetic-based techniques employ backscattering [10], radars [11], and Wi-Fi infrastructure [12] along with machine-learning techniques to classify different activities (walking, sitting, jumping, etc.). These are again restricted to closed/restricted environments and are focused on activity classification rather than precise motion monitoring (such as flexion and rotation). Inertial measurement units (IMUs) [13]–[15] break the laboratory boundaries but are unreliable (due to inherent drift) [13], [16] and not injury safe [17], [18]. Time-of-flight motion sensors that utilize ultrawideband radios [19] or ultrasonic [16] systems to determine the time taken for a launched pulse to travel from transmitter to receiver are again restricted by line of sight and are obtrusive. Bending sensors that are directly worn on the joint to measure the produced strain (monitored as change in the sensor's resistance [20] or permeability [21]) obstruct natural movement and can withstand only limited number of cycles. Recently, we reported a new class of coils that wrap around the individual's limb to monitor joint flexion [22] while overcoming the challenges above. Unfortunately, these coils 1) are restricted to only flexion monitoring; 2) are highly dependent on inter/intrasubject variability of limb geometry (i.e., anatomical circumference); and 3) suffer from poor resolution, especially at lower flexion angles (for instance, change of merely 0.11 dB is observed when the flexion angle changes from 0° to 10°). In this article, we introduce a new class of electrically small loop antennas (ESLAs) that are longitudinally placed upon the limbs [i.e., plane of the ESLA is parallel to the axis of the limb (Fig. 1)] to monitor motion while being robust to tissue variations and overcoming shortcomings in the state-of-the-art along with significantly outperforming our previously reported wrap-around coils [22] (Table I).

In this article, we begin with introducing the novel idea of employing ESLAs longitudinally across the joint to seamlessly monitor flexion and rotation. A two-ESLA configuration is discussed first, illuminating the merit of the idea, but indicating ambiguities under combined flexion and rotation scenarios for angular resolutions higher than 10°. To tackle this, a three-ESLA system with integrated post-processing is proposed, offering a resolution of 2° for combined flexion and rotation monitoring. The simulation results are presented and further validated by *in vitro* experiments. Guidelines for system

---

Manuscript received May 7, 2019; revised July 30, 2019; accepted August 8, 2019. Date of publication August 19, 2019; date of current version January 3, 2020. This work was supported by the National Science Foundation under Grant 1842531. *(Corresponding author: Vigyanshu Mishra.)*

The authors are with the ElectroScience Laboratory, Department of Electrical and Computer Engineering, The Ohio State University, Columbus, OH 43212 USA (e-mail: mishra.186@osu.edu; kiourti.1@osu.edu).

Color versions of one or more of the figures in this article are available online at http://ieeexplore.ieee.org.

Digital Object Identifier 10.1109/TAP.2019.2935147

TABLE I

COMPARISON OF APPROACHES FOR MONITORING JOINT KINEMATICS

	Camera Based	**Backscattering/ Radar/W-Fi Based**	**IMUs**	**Time-of-Flight**	**Bending Sensors**	**Wrap-Around Coils**	**Proposed**
Works in unconfined environment	No (-)	No (-)	Yes (+)	Yes (+)	Yes (+)	Yes (+)	Yes (+)
Seamless	Yes (+)	Yes (+)	No (-)	No (-)	Yes (+)	Yes (+)	Yes (+)
Insensitive to Line-of-Sight	No (-)	No (-)	Yes (+)	No (-)	Yes (+)	Yes (+)	Yes (+)
Allows natural motion	Yes (+)	Yes (+)	Yes (+)	Yes (+)	No (-)	Yes (+)	Yes (+)
Reliable vs. time	Yes (+)	Yes (+)	No (-)	Yes (+)	No (-)	Yes (+)	Yes (+)
Monitors Joint Flexion	Yes (+)	No (-)	Yes (+)	Yes (+)	Yes (+)	Yes (+)	Yes (+)
Monitors Joint Rotation	Yes (+)	No (-)	Yes (+)	Yes (+)	Yes (+)	No (-)	Yes (+)
Independent of anatomical geometry of limb	Yes (+)	Yes (+)	Yes (+)	Yes (+)	Yes (+)	No (-)	Yes (+)
Flexion dynamic range (0° to 100°)	-	-	-	-	-	14.24 dB	33.03 dB (18.79 dB improvement)
Lower flexion angles that can be detected at ~0.1 dB sensitivity	-	-	-	-	-	10°	1.5° (6.7 times improvement)

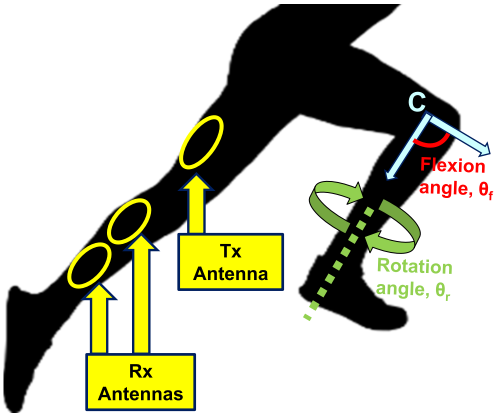

Fig. 1. ESLAs used to monitor joint flexion and rotation.

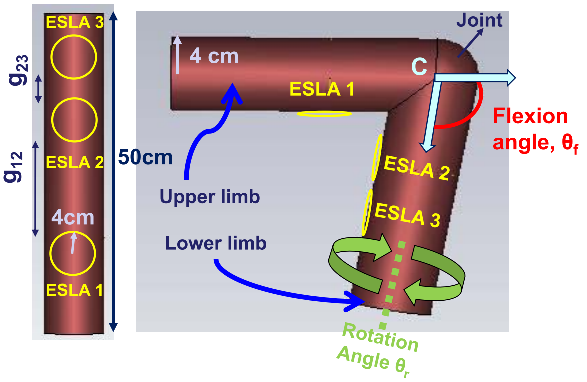

Fig. 2. Simulation setup consisting of cylindrical limb and spherical joint made of 2/3 muscle. ESLA 1 is used as Tx, while ESLAs 2 and 3 are used as Rx.

design suited to diverse applications are discussed, followed by studies that explore conformance to electromagnetic safety standards for the specific absorption rate (SAR).

II. OPERATING PRINCIPLE

As shown in Fig. 1, transmitter (Tx) and receiver (Rx) loop antennas are placed across the joint. Though focus of this article is on the knee joint, the approach is readily applicable to other joints as well. Flexion is achieved when the lower limb rotates with respect to the upper limb about the center "C" of the joint (Fig. 2). At full extension, limbs are straight and the flexion angle is zero, $\theta_\mathrm{f} = 0°$. As the lower limb flexes about the joint, flexion angle (θ_f) increases. Similarly, the lower limb may also rotate (by angle θ_r) about the joint. In both flexion and rotation scenarios, the transmitter and receiver antennas get misaligned, leading to changes in the associated transmission coefficient(s). In turn, such changes can be monitored to identify the exact flexion or/and rotation angles.

In principle, the system of Fig. 2 can be realized using three modes of operation, viz., 1) electrically large loops (circumference $\sim\lambda$, where λ represents wavelength); 2) electrically small loops (circumference $<0.1\lambda$) [23]; or 3) in between both modes of operation ($0.1\lambda <$ circumference $< \lambda$). Extensive frequency studies similar to those reported in [22] indicate that electrically small loops (ESLAs) operating at 34 MHz provide optimal performance in terms of: 1) received power levels; 2) resolution (smallest detectable angle); and 3) robustness to changes in tissue properties.

The operating principle can be better understood using Faraday's law of induction [24]

$$V_{Rx} = -\frac{d}{dt}\iint \boldsymbol{B_{Tx}} \cdot \widehat{n_{Rx}}\,ds \qquad (1)$$

where $\boldsymbol{B_{Tx}}$ is the transmitted magnetic flux density vector, $\widehat{n_{Rx}}$ is the receiver area vector, and $\mathrm{V_{Rx}}$ is the voltage induced on the receiver. Changes in flexion/rotation angle correspond to changes in the angle between $\widehat{n_{Rx}}$ and $\boldsymbol{B_{Tx}}$. This gets reflected in $\mathrm{V_{Rx}}$ and eventually captured in the transmission coefficient. That is, transmission coefficient becomes a function of flexion/rotation angle and, hence, can be used to monitor joint flexion and rotation.

As will be shown next, one transmitter and one receiver are enough to monitor joint flexion (at a given θ_r) or rotation (at a given θ_f). However, monitoring both flexion and rotation via a single transmitter/receiver pair leads to ambiguities for applications that require resolution higher than 10°. In other words, the same values of the transmission coefficient will end up corresponding to several different states of motion. To resolve ambiguities, two receiver antennas can be used. As such, Section III focuses on a two-ESLA configuration that will be used as a building block toward a three-ESLA configuration in Section IV.

III. TWO-ESLA CONFIGURATION

A. Simulations

The employed simulation setup is shown in Fig. 2, where ESLA 1 serves as Tx and ESLA 2 as Rx. A homogenous (2/3 of muscle properties [25], [26]) cylindrical model is used as a first-order approximation to human limbs, while the joint is modeled as a sphere. For this proof-of-concept model, the limb, joint, and ESLA radius are set to 4 cm. Copper wire is used to realize the ESLAs (0.254 mm in diameter), and a lumped capacitor (102 pF) is loaded on each of the ESLAs to introduce resonance and improve performance [22]. Gap between the ESLAs (g_{12}) in the extended state is set to 10 cm, in turn enabling flexion in the 0°–100° range. Flexion ($\theta_f = 0°–100°$) and rotation ($\theta_r = 0°–50°$) are then incorporated in the model. For simulations, the frequency domain solver of CST Microwave Studio (based on finite integral technique) is used with tetrahedral meshing.

Simulated transmission coefficients ($|S_{21}|$) at the resonance frequency of 34 MHz are shown in Fig. 3. To provide a complete picture, Fig. 3 plots indicative rotation curves ($\theta_r = 0°$, 40°, and 80°) along with indicative flexion curves ($\theta_f = 0°–100°$, at 10° steps). In this case, each rotation curve represents the change in $|S_{21}|$ as θ_r changes at a particular flexion angle. As an example, the rotation curve at $\theta_f = 80°$ is shown in the inset of Fig. 3. As expected, changes in flexion and/or rotation angle imply significant changes in $|S_{21}|$. In other words, $|S_{21}|$ can be monitored to assess joint flexion and rotation.

B. Experimental Validation

ESLAs of radius 4 cm are fabricated using 30 AWG (0.254 mm in diameter) copper wire and are further soldered to 102 pF lumped capacitors and SMA connectors [Fig. 4(a)]. To secure the coils, 3-D-printed fixtures with a groove are used [Fig. 4(a)]. The limb is realized using cylindrical Styrofoam of radius 4 cm, as enabled by the insensitivity of ESLAs' performance in the presence or absence of tissues (deduced from extensive frequency studies similar to [22]). A goniometer, commonly used to measure flexion angles in clinical practices, is inserted inside the upper/lower limbs [Fig. 4(b)]. The goniometer serves to emulate the flexing portion of the hinge joint while also assisting in setting up the intended flexion angle.

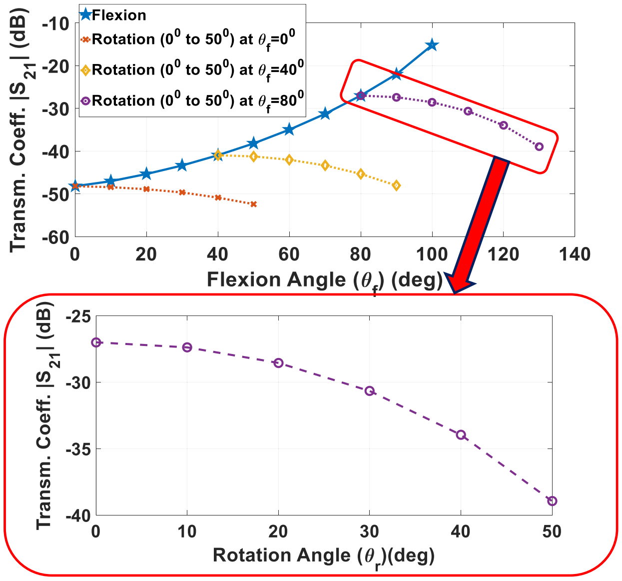

Fig. 3. Proof-of-concept results depicting changes in transmission coefficient ($|S_{21}|$) with varying flexion angle and rotation angle at 34 MHz. The bottom inset depicts an example rotation curve at $\theta_f = 80°$.

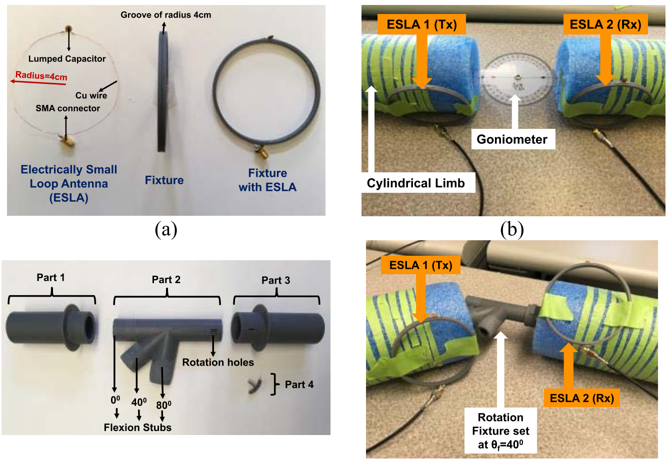

(a) (b)

(c) (d)

Fig. 4. (a) ESLA made of copper wire and subsequent integration in a 3-D-printed fixture with a groove. (b) Flexion measurement setup with goniometer, Styrofoam limbs, and ESLAs connected to a network analyzer. (c) Fixture devised to enable controllable flexion and rotation (the four parts are eventually combined into one). (d) Combined flexion and rotation measurement setup ($\theta_f = 40°$ and $\theta_r = 50°$).

To incorporate controllable rotation into the design, the fixture of Fig. 4(c) is devised and 3-D printed. The fixture consists of four parts: parts 1 and 3 are fixed in the upper and lower limbs, respectively; part 2 contains stubs for flexion at 0°, 40°, and 80° and holes for rotation from 0° to 50° at 10° steps; and part 4 helps fix the desired rotation angle by aligning the rotation holes between parts 2 and 3. Fig. 4(d) depicts an example setup with combined flexion and rotation ($\theta_f = 40°$ and $\theta_r = 50°$). To align with simulations, the fixture is designed such that the gap between the Tx and Rx ESLAs (g_{12}) is maintained at 10 cm for all flexion angles. For both flexion and rotation measurements, ESLAs are connected to the two ports of a PNA-L N5235A network analyzer.

The experimental results are shown in Fig. 5 and further superimposed with simulations. As seen, excellent agreement is achieved further validating the ESLA approach for monitoring flexion and rotation angles.

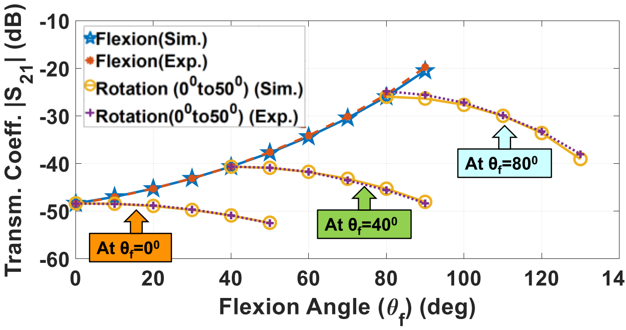

Fig. 5. Two-ESLA configuration: simulation and experimental results.

C. Ambiguity Considerations

As is clearly indicated in Fig. 5, there is no one-to-one correlation between the measured $|S_{21}|$ and associated flexion/rotation angles. For example, assuming a measurement of $|S_{21}| = -30$ dB, it is possible that ($\theta_{\mathrm{f}} = 70°$ and $\theta_{\mathrm{r}} = 0°$) or ($\theta_{\mathrm{f}} = 80°$ and $\theta_{\mathrm{r}} = 30°$), among others. Nevertheless, and as will become clear in Section IV-B, it is still possible to monitor both flexion and rotation using this configuration for applications that require resolution down to 10°. However, for applications that require higher resolution, ambiguities arise in deciphering the right position of the limb. To tackle this, a three-ESLA configuration with integrated post-processing is discussed next. The results of Fig. 5 are, in turn, used as a building block toward the three-ESLA design.

IV. Three-ESLA Configuration

A. Operating Principle

Using the three-ESLA configuration of Fig. 2, where ESLA 1 serves as Tx and ESLAs 2 and 3 as Rx, the same flexion and rotation angles are now captured by two different receivers. Notably, these receivers are asymmetrically positioned with respect to the transmitter, implying that asymmetric trends are anticipated in the $|S_{21}|$ and $|S_{31}|$ values. This is demonstrated in Section IV-B. In turn, ambiguous (θ_{f}, θ_{r}) pairs arising by the $|S_{21}|$ and $|S_{31}|$ curves will not be the same. Ideally, there should be only a single flexion/rotation angle combination that is identified by both $|S_{21}|$ and $|S_{31}|$ plots, and this will be the true and desired reading. This is discussed in Section IV-C.

B. Simulation and Experimental Results

Simulations are carried out using the three-ESLA configuration of Fig. 2. For this proof-of-concept design, ESLAs 2 and 3 are separated by a gap (g_{23}) of 2 cm, while ESLAs 1 and 2 are separated by a gap (g_{12}) of 10 cm. Simulations are carried out for $\theta_{\mathrm{f}} = 0°$–$100°$ (at steps of 10°) and $\theta_{\mathrm{r}} = 0°$–$50°$ (at steps of 10° and at $\theta_{\mathrm{f}} = 0°, 40°$, and $80°$). Corresponding experiments are performed on the Styrofoam phantom of Fig. 4. For flexion-only monitoring, the employed setup is shown in Fig. 6(a) where an inserted goniometer helps set the flexion angle. For combined flexion/rotation monitoring, the 3-D-printed fixture of Fig. 4 is employed, as shown in Fig. 6(b). Transmission coefficient values are measured using a two-port network analyzer, one receiver at a time. While taking $|S_{21}|$ measurements, ESLA 3 is terminated with a 50 Ω load, and vice versa. This accounts for practical scenarios where both receivers are connected to 50 Ω rather than being left open. The simulation and experimental results are depicted in Fig. 6(c) and are in excellent agreement.

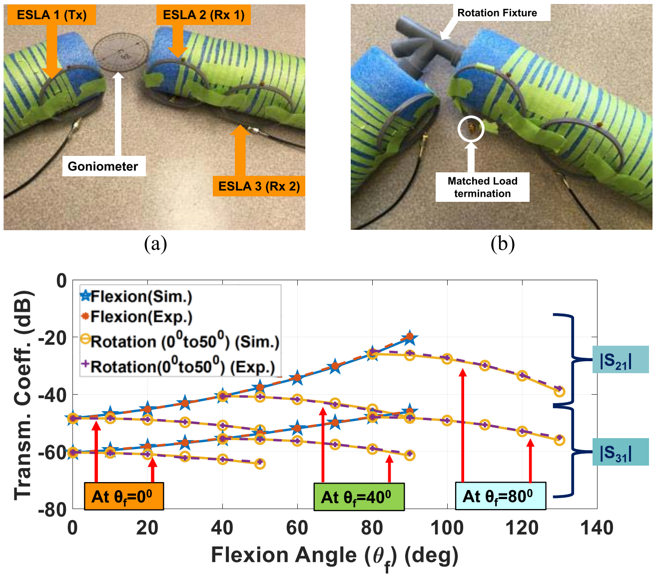

(a) (b)

(c)

Fig. 6. Three-ESLA configuration. Measurement setup for (a) flexion monitoring using a goniometer and (b) combined flexion and rotation monitoring using an in-house fixture. (c) Simulation and experimental results.

C. Resolving Ambiguities

To evaluate the feasibility of resolving ambiguities, simulations are carried out for $\theta_{\mathrm{f}} = 0°$–$100°$ (at 10° steps) and $\theta_{\mathrm{r}} = 0°$–$50°$ (at 10° steps, and at $\theta_{\mathrm{f}} = 0°$–$100°$ at 10° steps). The step size of 10° throughout these simulations sets the system resolution to 10° and leads to a total of 132 data points (i.e., $|S_{21}|$ and $|S_{31}|$ values). With precision set to two decimal digits, post-processing is performed in MATLAB to identify ambiguities in $|S_{21}|$ and $|S_{31}|$, and resolve them as needed. For a system resolution of 10°, no ambiguities are identified, implying that just a two-ESLA configuration is sufficient in this case. For a system resolution of lower than 10°, similar behavior is expected.

Similar tests are subsequently performed at higher system resolutions (Table II). As expected, ambiguities arise for both $|S_{21}|$ and $|S_{31}|$, with the number of ambiguities increasing at higher resolutions. Notably, no overlap is found in the ambiguities of $|S_{21}|$ versus the ambiguities of $|S_{31}|$ for resolutions as high as 2°. That is, the three-ESLA configuration is able to resolve ambiguities within a system resolution of as high as 2°. For resolutions higher than 2°, ambiguities cannot be resolved (Table II). This can be surmounted: 1) by using more than two Rx coils or 2) by judicious selection of the ESLA radius and gap (g_{12}), both of which play a crucial role in controlling the resolution per Section V. Of course, the aforementioned results are tied to the two decimal

TABLE II

POSTPROCESSING FOR DIFFERENT ANGULAR RESOLUTIONS

Resolution	Total Data Points	Number of Ambiguities		Ambiguity Overlaps
		$\lvert S_{21}\rvert$	$\lvert S_{31}\rvert$	
10°	132	0	0	0
5°	462	1	1	0
3.3°	992	3	3	0
2.5°	1722	13	15	0
2°	2652	25	21	0
1.67°	3782	29	54	1
1.43°	5112	53	75	1
1.25	6642	88	137	1
1.11°	8372	109	221	5
1°	10302	179	252	10

precision selected above. The number of ambiguous (θ_{f} and θ_{r}) pairs is anticipated to decrease with higher precision.

V. PERFORMANCE METRICS

Key performance metrics are hereafter identified and analyzed, aiming to serve as guidelines for system design suited to diverse applications in future. For simplicity purposes, the two-ESLA system is considered first, followed by discussions on applicability to the three-ESLA system.

A. Resolution

Resolution is governed by the dynamic range of transmission coefficient values across a desired range of flexion/rotation angles. Higher dynamic ranges lead to finer discrimination of angular values, hence improving resolution. Of course, this is valid only because the transmission coefficient curves are monotonically increasing/decreasing functions. Note that, dynamic range and resolution are not completely analogous here, as the slope is not constant throughout. However, since the slope does not drastically change, it does provide a good measure as a first-order approximation for quantification and comparison purposes.

As seen in Fig. 5, slope of the flexion/rotation curves at lower angles is lower as compared to higher angles. This reduces the dynamic range and, hence, the resolution at lower angles. Added to the above, this reduced dynamic range increases the chances of (θ_{f}, θ_{r}) ambiguities at lower angles and, in turn, increases the difficulty in resolving them. In fact, for all resolution tests performed beyond 2°, all overlaps occur at $\theta_{\mathrm{f}} < 30°$. Nevertheless, fine-tuning of g_{12}, ESLA radius, and/or operation frequency may control/improve resolution, as outlined below.

1) Fine-Tuning the ESLA Gap: Considering g_{12} as the design parameter and for flexion-only scenario ($\theta_{\mathrm{f}} = 0°$), Fig. 7(a) plots flexion curves ($|S_{21}|$ versus θ_{f}) for different values of gaps (g_{12}). As seen, slope or dynamic range improves with decreasing g_{12}. To better visualize this, Fig. 7(b) plots the $|S_{21}|$ dynamic range (across $\theta_{\mathrm{f}} = 0°–60°$ and $\theta_{\mathrm{f}} = 0°–20°$) as a function of g_{12}. Indeed, the dynamic range significantly improves with the decrease in g_{12} even at smaller angles. The quantitative results are shown in Table III and are further compared versus those of our previously reported wrap-around coils [22]. As seen, significant improvement is achieved.

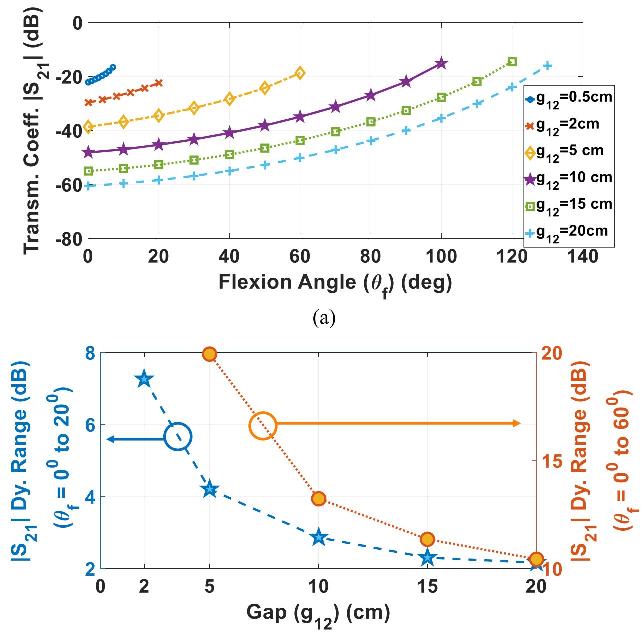

(a)

(b)

Fig. 7. (a) Flexion curves for different values of gaps (g_{12}). (b) Increase in dynamic range (for both $\theta_{\mathrm{f}} = 0°–20°$ and $\theta_{\mathrm{f}} = 0°–60°$) with the decrease in g_{12}.

TABLE III

COMPARISON OF DYNAMIC RANGE

g_{12} (cm)	θ_{f} (deg)	$\lvert S_{21}\rvert$ Dynamic Range (dB)		
		[22]	This work	Improvement
20	0° to 130°	22.1	44.6	22.5
	0° to 60°	2.62	10.43	7.81
	0° to 20°	0.16	2.16	2
10	0° to 100°	14.24	33.03	18.79
	0° to 60°	3.26	13.23	9.97
	0° to 20°	0.36	2.86	2.5
5	0° to 60°	6.2	19.92	13.72
	0° to 20°	0.46	4.2	3.74
2	0° to 20°	1.24	7.26	6.02
	0° to 5°	0.07	1.44	1.37
0.5	0° to 5°	0.4	3.19	2.79
	0° to 1°	0.01	0.52	0.51
	0° to 0.1°	-	0.04	-

For rotation, top image of Fig. 8(a) depicts the dynamic range variation versus g_{12} at different θ_{f}, while bottom image of Fig. 8(a) depicts the dynamic range variation versus θ_{f} at different g_{12}. At high θ_{f}, the decrease in g_{12} helps improve the dynamic range (regardless of θ_{r}); however, it is not much useful at smaller θ_{f}. Also, it can be inferred that dynamic range for rotation is a function of both g_{12} and θ_{f}. Hence, Fig. 8(b) shows the intuitive effect of both parameters, depicting better dynamic range/resolution at higher θ_{f} and smaller g_{12}.

Following these guidelines, resolution of the three-ESLA configuration of Fig. 2 may increase to 0.4° for $g_{12} = 3$ cm as compared to 2° for $g_{12} = 10$ cm. Thus, using g_{12} as a design parameter, resolution of the complete system can be tweaked as required.

2) Fine-Tuning the ESLA Radius: Assuming a flexion-only scenario ($\theta_{\mathrm{f}} = 0°$), Fig. 9(a) plots flexion curves for different ESLA radii, while Fig. 9(b) plots the corresponding dynamic range. As seen, the decrease in radius leads to better dynamic range for all θ_{f} values.

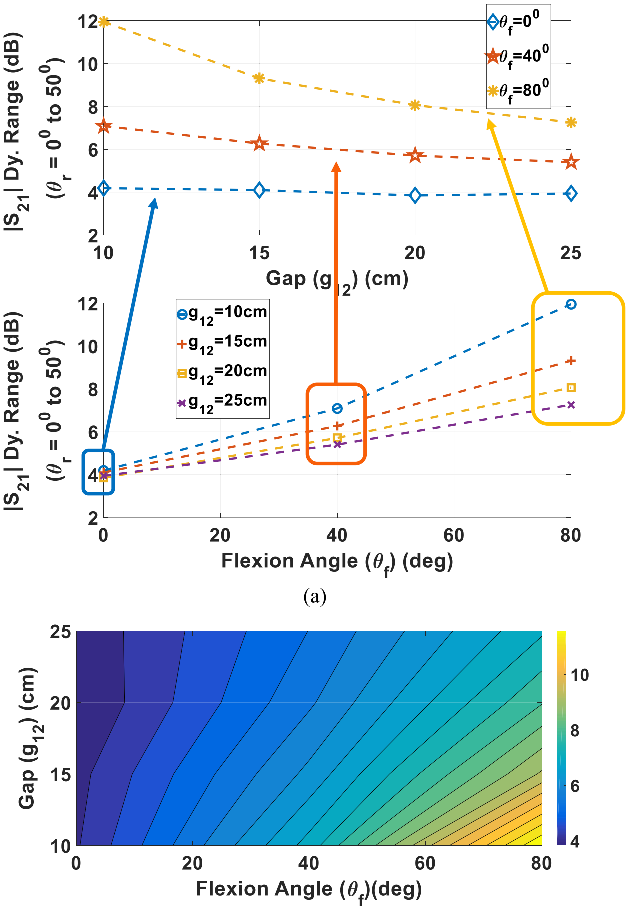

Fig. 8. (a) Dynamic range $|S_{21}|$ variation for rotation ($\theta_r = 0°–50°$) with θ_f for different values of gap (g_{12}) and with gap (g_{12}) for different values of θ_f. (b) Contour plot depicting the variation with both g_{12} and θ_f simultaneously. Better range is obtained for smaller g_{12} and larger θ_f.

For rotation, radius variations depict very similar trends as those of g_{12} variations (Fig. 10). That is, better rotation resolution can be achieved at higher θ_f and at smaller radius values. The reason for this similar trend can be attributed to the fact that in both cases reduction in g_{12} or radius leads to more drastic changes in flux linkage with angular variation.

Similar to g_{12}, radius reduction will also help improve the resolution of the three-ESLA configuration of Fig. 2. Since the effect of both parameters is similar, analyses performed for g_{12} are not shown to avoid redundancy.

3) Fine-Tuning the Frequency: Considering frequency as a design parameter, similar to the discussion reported in [22], lower frequency of operation leads to better flexion resolution. This is also one of the reasons behind the selection of 34 MHz as the optimal operating frequency. However, frequency selection has relatively negligible effect on the rotation resolution.

B. Range of Motion and Power Reception

Range of motion (ROM) relates to the range of flexion (θ_f) and/or rotation (θ_r) angles. Ideally, higher ROM is desirable. With the present configuration of two and three ESLAs, there is no limit on the rotation ROM irrespective of g_{12}, radius, or θ_f variation. However, the decrease in g_{12} leads to reduction in flexion ROM as depicted in Fig. 7(a). This is because reduction in g_{12} results in transmit and receive ESLAs physically touching each other. Radius variation, on other hand, does not restrict flexion ROM [Fig. 9(a)].

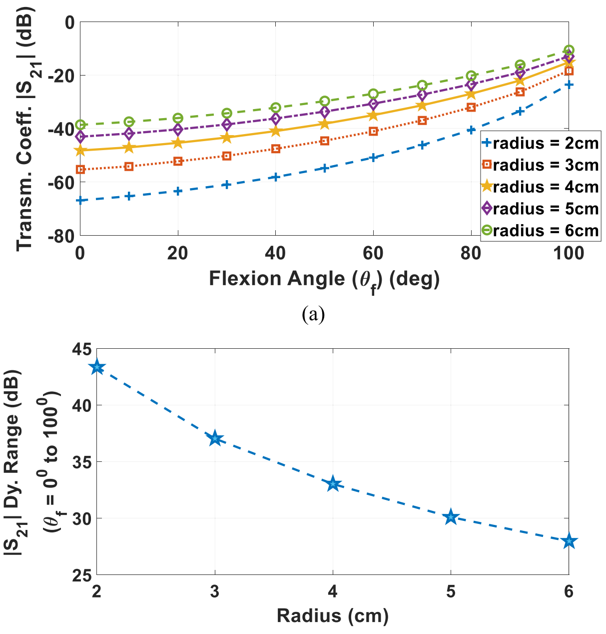

Fig. 9. (a) Flexion curves for different values of radius. (b) Increase in dynamic range ($|S_{21}|$) for flexion $\theta_f = 0°–100°$ with the decrease in radius.

Power levels received by the Rx ESLA(s) are desired to be as high as possible. As is evident from Figs. 7(a) and 9(a), power reception improves with the decrease in g_{12} and increase in radius. Similar trends are observed for the rotation curves as well.

In a nutshell, by decreasing g_{12}, power reception and resolution increase but ROM decreases. By decreasing the ESLA radius, power reception reduces, resolution increases, and ROM remains unaffected. These imply a tradeoff in the design, a conclusion which is equally valid for the three-ESLA system.

C. Insensitivity to Tissue Variation

System performance should be independent of tissue variations. An analysis similar to that performed in [22] has been repeated for the proposed ESLAs, indicating that frequencies in the inductive region are again suitable to meet this requirement. This is yet another reason for the choice of 34 MHz as the optimal operating frequency.

D. Specific Absorption Rate Studies

To ensure conformance with international safety guidelines, SAR studies are performed. The multi-layer arm model reported in [22] is employed, consisting of 1.17 mm-thick skin, 6.63 mm-thick fat, 21.45 mm-thick muscle, 4.68 mm-thick cortical bone, and 5.07 mm bone. For the two- and three-ESLA configurations, and assuming an input power of –15 dBm (as used in the experiments), maximum SAR averaged over 1 g of tissue is equal to 1.44 μW/Kg. This value is extremely low as compared to the safety limit of 1.6 W/Kg set by Federal Communications Commission (FCC).

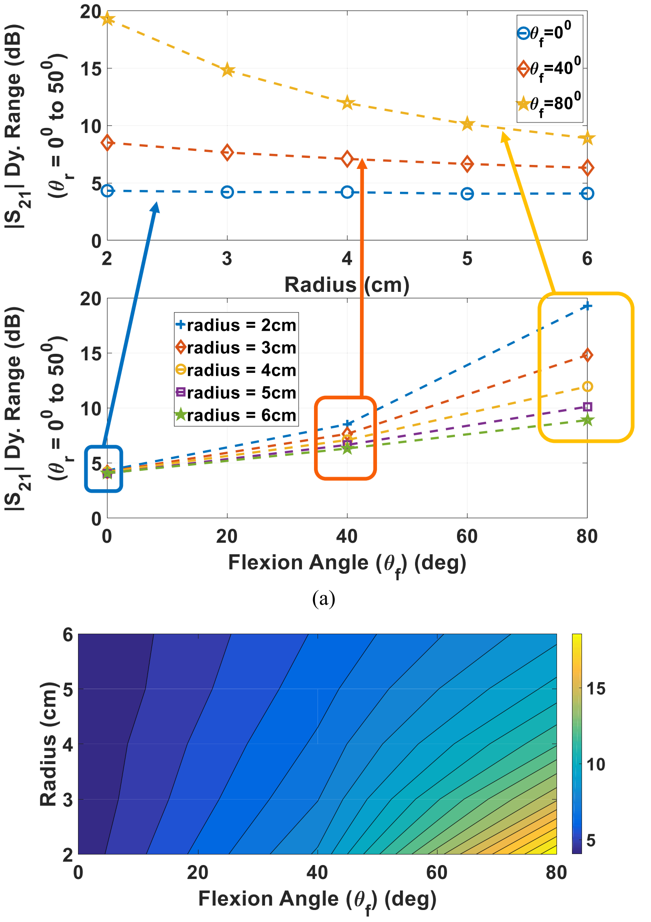

Fig. 10. (a) Dynamic range $|S_{21}|$ variation for rotation ($\theta_r = 0°–50°$) with θ_f for different values of radius and with radius for different values of θ_f. (b) Contour plot depicting the variation with both radius and θ_f simultaneously. Better range is obtained for smaller radius and larger flexion angles.

E. Error and Noise Considerations

Error and noise considerations become important, particularly when the system is intended to operate in dynamic or noisy environments. To this end, a noise tolerance analysis is hereafter performed that estimates the error handling capability of the system. Here, it is worth noting that the reported system is not designed for optimal noise tolerance capability. In other words, sensing of joint flexion/rotation via longitudinal ESLAs is not restricted to this analysis, and system design may readily be optimized in future for higher noise tolerance. However, our analysis does provide a baseline performance for noise tolerance.

Assuming operation in dynamic settings, the experimental data obtained can be compared versus the calibration data to identify possible (θ_f, θ_r) values. In turn, noise tolerance can be determined from the calibration data themselves. In the following, simulation data are used as a calibration reference to perform this analysis. For a given system resolution and for a given data point ($|S_{21}|$) at a given θ_f or θ_r, half of the distance from that data point on either side will set the noise tolerance limit for that point. Now, if the noise in the experimental data exceeds this limit for that specific data point, the corresponding angle pair (θ_f, θ_r) obtained will be in error. In turn, this will lead to error in identifying the state of motion after post-processing. Reiterating this idea for all data points corresponding to each θ_f and θ_r, and for different resolutions, noise tolerance can be generated as shown in Fig. 11(a) and (b).

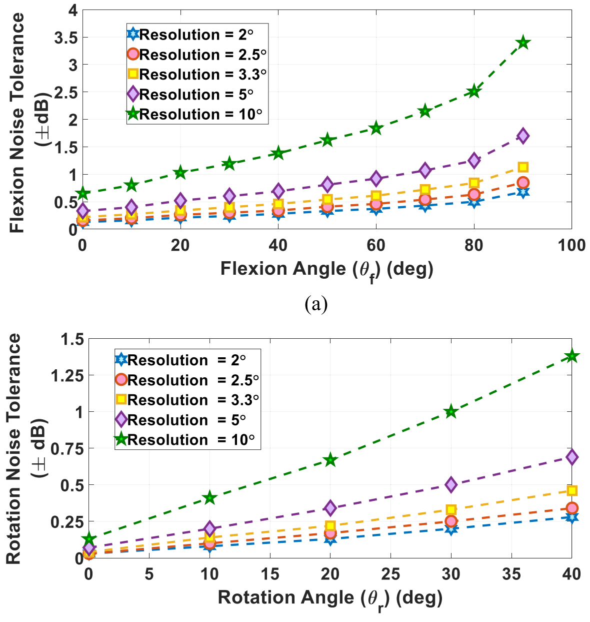

Fig. 11. Noise tolerance (±dB) for (a) flexion and (b) rotation corresponding $|S_{21}|$, depicting the decrease in chances of error as angle increases and resolution decreases.

As expected, noise tolerance increases with increasing θ_f and θ_r (since |slope| of $|S_{21}|$ versus θ_f or θ_r increases with increasing θ_f or θ_r). Further, tolerance improves with the decrease in system resolution, showing a tradeoff between the two. A similar analysis can be performed for $|S_{31}|$ data.

VI. CONCLUSION

In this article, a unique configuration of wearable ESLAs was introduced for seamlessly monitoring joint flexion and rotation. The reported approach 1) has the potential to break laboratory boundaries and enable monitoring in the individual's natural environment; 2) is not restricted by line-of-sight concerns (unlike optical cameras and time-of-flight sensors); 3) does not restrict natural motion (unlike bending sensors); 4) does not drift (unlike IMUs); and 5) can monitor both flexion and rotation (unlike wrap-around coils).

A two-ESLA configuration was reported first, able to monitor flexion and rotation at resolutions of 10° or lower. However, ambiguities were shown to arise for applications that require higher resolution. To tackle this, a three-ESLA configuration with accompanying post-processing was reported, achieving resolution of as high as 2° at an example distance of 10 cm between the coils. Guidelines for system design suited to diverse applications in future indicated that resolution may be further improved by fine-tuning the ESLA radius, ESLA separation, and ESLA operation frequency. Nevertheless, inherent tradeoffs were identified in power reception and ROM, which should be carefully accounted for during the design process.

The system may eventually be utilized for seamless motion capture in applications as diverse as healthcare, sports, virtual reality, human–machine interfaces, and gesture recognition, among others. Future work will focus on: 1) implementing the ESLAs on flexible e-textiles; 2) making the system wireless and portable; 3) validating *in vivo*; and 4) optimizing the system for higher noise tolerance in dynamic and real-world environments.

REFERENCES

[1] C. Godinho *et al.*, "A systematic review of the characteristics and validity of monitoring technologies to assess Parkinson's disease," *J. NeuroEng. Rehabil.*, vol. 13, no. 1, Mar. 2016, Art. no. 24.

[2] V. Bonnet, V. Joukov, D. Kulić, P. Fraisse, N. Ramdani, and G. Venture, "Monitoring of hip and knee joint angles using a single inertial measurement unit during lower limb rehabilitation," *IEEE Sensors J.*, vol. 16, no. 6, pp. 1557–1564, Mar. 2016.

[3] T. P. Luu, Y. He, S. Brown, S. Nakagome, and J. L. Contreras-Vidal, "Gait adaptation to visual kinematic perturbations using a real-time closed-loop brain–computer interface to a virtual reality avatar," *J. Neural Eng.*, vol. 13, no. 3, Apr. 2016, Art. no. 036006.

[4] Y. Xiao, Z. Zhang, A. Beck, J. Yuan, and D. Thalmann, "Human–robot interaction by understanding upper body gestures," *Presence, Teleoperators Virtual Environ.*, vol. 23, no. 2, pp. 133–154, 2014.

[5] H. Wagner, J. Pfusterschmied, M. Tilp, J. Landlinger, S. P. von Duvillard, and E. Müller, "Upper-body kinematics in team-handball throw, tennis serve, and volleyball spike," *Scand. J. Med. Sci. Sports*, vol. 24, no. 2, pp. 345–354, Apr. 2014.

[6] P. Eichelberger *et al.*, "Analysis of accuracy in optical motion capture—A protocol for laboratory setup evaluation," *J. Biomech.*, vol. 49, no. 10, pp. 2085–2088, Jul. 2016.

[7] L. Herda, P. Fua, R. Plänkers, R. Boulic, and D. Thalmann, "Using skeleton-based tracking to increase the reliability of optical motion capture," *Hum. Movement Sci.*, vol. 20, no. 3, pp. 313–341, Jun. 2001.

[8] E. E. Stone and M. Skubic, "Unobtrusive, continuous, in-home gait measurement using the Microsoft Kinect," *IEEE Trans. Biomed. Eng.*, vol. 60, no. 10, pp. 2925–2932, Oct. 2013.

[9] F. Ferryanto and M. Nakashima, "Development of a markerless optical motion capture system for daily use of training in swimming," *Sports Eng.*, vol. 20, no. 1, pp. 63–72, Mar. 2017.

[10] S. Amendola, L. Bianchi, and G. Marrocco, "Movement detection of human body segments: Passive radio-frequency identification and machine-learning technologies," *IEEE Antennas Propag. Mag.*, vol. 57, no. 3, pp. 23–37, Jun. 2015.

[11] F. Qi *et al.*, "Position-information-indexed classifier for improved through-wall detection and classification of human activities using UWB bio-radar," *IEEE Antennas Wireless Propag. Lett.*, vol. 18, no. 3, pp. 437–441, Mar. 2019.

[12] J. Liu, L. Wang, J. Fang, L. Guo, B. Lu, and L. Shu, "Multi-target intense human motion analysis and detection using channel state information," *Sensors*, vol. 18, p. 3379, Oct. 2018.

[13] M. El-Gohary and J. McNames, "Shoulder and elbow joint angle tracking with inertial sensors," *IEEE Trans. Biomed. Eng.*, vol. 59, no. 9, pp. 2635–2641, Sep. 2012.

[14] F. A. de Magalhaes, G. Vannozzi, G. Gatta, and S. Fantozzi, "Wearable inertial sensors in swimming motion analysis: A systematic review," *J. Sports Sci.*, vol. 33, no. 7, pp. 732–745, 2015.

[15] B. Mariani, M. C. Jiménez, F. J. G. Vingerhoets, and K. Aminian, "On-shoe wearable sensors for gait and turning assessment of patients with Parkinson's disease," *IEEE Trans. Biomed. Eng.*, vol. 60, no. 1, pp. 155–158, Jan. 2013.

[16] C. Einsmann, M. Quirk, B. Muzal, B. Venkatramani, T. Martin, and M. Jones, "Modeling a wearable full-body motion capture system," in *Proc. IEEE 9th Int. Symp. Wearable Comput. (ISWC)*, Osaka, Japan, Oct. 2005, pp. 144–151.

[17] S. C. Mukhopadhyay, "Wearable sensors for human activity monitoring: A review," *IEEE Sensors J.*, vol. 15, no. 3, pp. 1321–1330, Mar. 2015.

[18] T. Shany, S. J. Redmond, M. R. Narayanan, and N. H. Lovell, "Sensors-based wearable systems for monitoring of human movement and falls," *IEEE Sensors J.*, vol. 12, no. 3, pp. 658–670, Mar. 2012.

[19] Y. Qi, C. B. Soh, E. Gunawan, K.-S. Low, and A. Maskooki, "A novel approach to joint flexion/extension angles measurement based on wearable UWB radios," *IEEE J. Biomed. Health Informat.*, vol. 18, no. 1, pp. 300–308, Jan. 2014.

[20] J. H. M. Bergmann, S. Anastasova-Ivanova, I. Spulber, V. Gulati, P. Georgiou, and A. McGregor, "An attachable clothing sensor system for measuring knee joint angles," *IEEE Sensors J.*, vol. 13, no. 10, pp. 4090–4097, Oct. 2013.

[21] G. Moreton, T. Meydan, and P. Williams, "Investigation and characterization of a planar figure-of-eight coil as a curvature sensor," in *Proc. IEEE SENSORS*, Glasgow, U.K., Oct./Nov. 2017, pp. 1–3.

[22] V. Mishra and A. Kiourti, "Wrap-around wearable coils for seamless monitoring of joint flexion," *IEEE Trans. Biomed. Eng.*, to be published. doi: 10.1109/TBME.2019.2895293.

[23] C. A. Balanis, "Loop antennas," in *Antenna Theory Analysis and Design*, 4th ed. Hoboken, NJ, USA: Wiley, 2016.

[24] W. H. Hayt, Jr., and J. A. Buck, "Time-varying fields and Maxwell's equations," in *Engineering Electromagnetics*, 6th ed. New York, NY, USA: McGraw-Hill, 2001.

[25] C. Furse, D. A. Christensen, and C. H. Durney, "Electric and magnetic fields: Basic concepts," in *Basic Introduction to Bioelectromagnetics*, 2nd ed. Boca Raton, FL, USA: CRC Press, 2009, pp. 30–34.

[26] P. Soontornpipit, C. M. Furse, and Y. C. Chung, "Design of implantable microstrip antenna for communication with medical implants," *IEEE Trans. Microw. Theory Techn.*, vol. 52, no. 8, pp. 1944–1951, Aug. 2004.

Vigyanshu Mishra (S'18) received the B.Tech. degree in electronics and communication engineering from PDPM Indian Institute of Information Technology, Design and Manufacturing, Jabalpur, Madhya Pradesh, India, in 2012 and the M.Tech. degree in radio frequency design and technology from Indian Institute of Technology Delhi, New Delhi, India, in 2015. He is currently pursuing the Ph.D. degree in electrical and electronics engineering from the ElectroScience Laboratory, The Ohio State University, Columbus, OH, USA, under the supervision of Dr. A. Kiourti.

He has held research positions on different research projects at the Center for Applied Research in Electronics, IIT Delhi, and has served as an Engineer with Wireless Planning and Coordination Wing, New Delhi, and Wireless Monitoring Organization, Ahmedabad, India, Ministry of Communication and IT, Government of India, New Delhi. He has researched on various aspects of electromagnetics. He has authored four journal papers and six conference papers. His current research interests include electromagnetics for wearable and biomedical applications.

Mr. Mishra was a recipient of several awards and fellowships, including the IEEE Microwave Theory and Techniques Society (MTT-S) Graduate Fellowship for Medical Applications for 2019, the USNC-URSI 2019 Travel Fellowship, and the University Fellowship for the year 2017–2018 by The Ohio State University.

Asimina Kiourti (S'10–M'14–SM'19) received the Diploma degree in electrical and computer engineering from the University of Patras, Patras, Greece, in 2008, the M.Sc. degree in technologies for broadband communications from University College London, London, U.K., in 2009, and the Ph.D. degree in electrical and computer engineering from the National Technical University of Athens, Athens, Greece, in 2013.

From 2013 to 2014, she worked as a Post-Doctoral Researcher at the ElectroScience Laboratory, The Ohio State University, Columbus, OH, USA, and from 2014 to 2016, she was a Senior Research Associate at the same school. In 2016, she joined the faculty of The Ohio State University as an Assistant Professor of electrical and computer engineering. She has authored more than 50 journal papers, 80 conference papers, and 9 book chapters. She holds 3 patents. Her current research interests include bioelectromagnetics, wearable and implantable antennas, sensors for body area applications, and functionalized e-textiles.

Dr. Kiourti was a recipient of several awards and scholarships, including the URSI Young Scientist Award in 2018, the IEEE Engineering in Medicine and Biology Society (EMB-S) Young Investigator Award in 2014, the IEEE Microwave Theory and Techniques Society (MTT-S) Graduate Fellowship for Medical Applications in 2012, and the IEEE Antennas and Propagation Society (AP-S) Doctoral Research Award in 2011. She is currently serving as an Associate Editor for the IEEE TRANSACTIONS ON ANTENNAS AND PROPAGATION, the IEEE JOURNAL OF ELECTROMAGNETICS, RF AND MICROWAVES IN MEDICINE AND BIOLOGY, and *Advanced Electromagnetics*.